may have been admixed to the Moon after it formed, perhaps the equivalent of the late veneer on Earth. Although evidence of large impacts is still visible on the surface of the Moon, we have not found any indication of meteoritic material admixed to any of our lunar samples using oxygen isotopes. This does not exclude addition of meteoritic material completely but does limit the amount to several percent. The proportions can be calculated for different meteorite classes. The high (H), low (L), and very low (LL) iron ordinary chondrites are displaced from the TFL by +0.7, +1.0, and +1.3‰ on average (*5*). Admixing 3% H-chondritic material, for example, would be detectable when 0.016‰ deviation is considered significant (Fig. 3). Even less material from L or LL or carbonaceous chondrites would be detectable because these groups are further displaced from the TFL. Although CI-chondrites plot on the TFL, this group is characterized by high $\delta^{18}O$ values above 16‰. Any proportion larger than 5% would increase the $\delta^{18}O$ value by at least 0.5‰. This is also not found for any of the analyzed rocks. Planetesimals with a similar $\Delta^{17}O$ as Mars admixed to any of the lunar samples would need to be present in proportions of >5% to be detectable using oxygen isotopes (Fig. 3). Therefore, we can exclude the possibility that >3 and >5% of these primitive meteoritic or differentiated planetesimals, respectively, have been admixed to any of the studied lunar samples. The only meteorites that are difficult to exclude are the highly reduced enstatite chondrites and aubrites. These have $\Delta^{17}O$ and $\delta^{18}O$ values either identical or very similar to Earth and the Moon (*23*, *24*) and, therefore, could have contributed more than 5% to lunar rocks.

References

1. A. G. W. Cameron, W. Benz, *Icarus* **92**, 204 (1991).
2. A. G. W. Cameron, R. M. Canup, *Lunar Planet Sci* **XXIX**, 1062 (1998); R. M. Canup, E. Asphaug, *Nature* **412**, 708 (2001).
3. A. N. Halliday, *Earth Planet. Sci. Lett.* **176**, 17 (2000a).
4. R. N. Clayton, T. K. Mayeda, *Proc Lunar Sci Conf* **XI**, 1761 (1975).
5. ———, *Geochim. Cosmochim. Acta* **60**, 1999 (1996).
6. Z. D. Sharp, *Geochim. Cosmochim. Acta* **54**, 1353 (1990).
7. D. Rumble III, J. Farquhar, E. D. Young, C. P. Christensen, *Geochim. Cosmochim. Acta* **61**, 4229 (1997).
8. The oxygen isotope ratios of lunar rocks were measured at the Geophysical Laboratory, Carnegie Institution using a Synrad Series 48 CO_2 laser (Synrad, Inc.; Mukilteo, WA) (*6*, *7*). For some samples 1 to 5 small fragments (f) with a total mass between 1.5 and 2.5 mg were reacted in a BrF_5 atmosphere. Powdered samples (p) were melted in vacuum before fluorination in order to avoid losing material by violent reaction of the powder with BrF_5 during laser heating. Surplus BrF_5 and other condensable gases were frozen in liquid nitrogen cold traps. Oxygen was transferred by a Hg-diffusion pump from the metal to the glass line and was frozen on a liquid nitrogen–cooled 5 Å molecular sieve. The function of the diffusion pump is twofold (i) the transport time of oxygen from the sample chamber to the 5 Å molecular sieve is significantly reduced and (ii) tiny amounts of fluorine species (sometimes flushed with the oxygen through the cold traps) are removed by reaction with hot mercury. The isotopic composition was measured on mass 32, 33, and 34 on a MAT-252 dynamic gas source mass spectrometer (Thermo Finnigan MAT; Bremen, Germany). No corrections on mass 33 ($^{17}O^{16}O$) were made because the high-mass resolution of the MAT-252 reduces scattering of $^{32}O_2^-$. The compounds NF_3 and CF_4, which may be produced as by-products during laser fluorination, are known to cause mass interferences at a mass-to-charge ratio (*m/e*) of 33 ($^{17}O^{16}O$) or otherwise interfere with analysis. These compounds were eliminated by preferential adsorption on the 5 Å molecular sieve (*7*). Routine monitoring of these compounds during each analysis by scanning *m/e* 52 (NF_2^+) and 69 (CF_3^+) showed that they were undetectable. The $\delta^{18}O$ value of the reference oxygen has been calibrated to the standard mean ocean water (SMOW) scale with the use of UWG-2, a garnet standard from the University of Wisconsin (*9*). The recommended $\delta^{18}O$ value of UWG-2 is 5.80‰ relative to NIST SRM-28 = 9.60‰. UWG-2 has also been used to define the $\delta^{17}O$ value of the oxygen reference using a value of +3.04‰ on the $\delta^{17}O$ SMOW scale. This value has been calculated from a slope of 0.5245 for the terrestrial fractionation line as defined by 11 minerals with a large range of $\delta^{18}O$ values from 0 to 12‰ and the $\delta^{18}O$ value of UWG-2 using the equation $\delta^{17}O_{(UWG\text{-}2)} = \delta^{18}O_{(UWG\text{-}2)} * 0.5245$. This equation cannot simply be applied to the oxygen reference gas because the reference gas does lie off the terrestrial fractionation line ($\Delta^{17}O = -0.47‰$).
9. J. Valley, N. Kitchen, M. J. Kohn, C. R. Niendorf, M. Spicuzza, *Geochim. Cosmochim. Acta* **59**, 5223 (1995).
10. We first analyzed terrestrial samples with a wide range of $\delta^{18}O$ from about 0 to 12‰ to be able to detect very small deviations from the mass-dependent terrestrial fractionation line. The linear equation calculated for the terrestrial samples in $\delta^{17}O - \delta^{18}O$ space is $\delta^{17}O = 0.5245 \pm 0.0008 = \delta^{18}$ (2σ confidence level) with a squared correlation coefficient of $R^2 = 0.9999$. Mass-independent displacements are expressed relative to this experimentally determined terrestrial fractionation line as $\Delta^{17}O = \delta^{17}O - 0.5245 * \delta^{18}O$. A terrestrial olivine standard was analyzed together with the lunar samples in every run. Ten analyses of this olivine average $\Delta^{17}O = -0.003 \pm 0.017$ ‰ and 11 analyses of UWG-2 gives 0.001 ± 0.010‰. The overall $\Delta^{17}O$ average of the terrestrial samples is 0.003 ± 0.008‰.
11. J. M. Eiler, P. Schiano, N. Kitchen, E. M. Stolper, *Science* **403**, 530 (2000).
12. I. A. Franchi, I. P. Wright, A. S. Sexton, T. Pillinger, *Meteorit. Planet. Sci.* **34**, 657 (1999).
13. A. G. W. Cameron, *Meteorit. Planet. Sci.* **36**, 9 (2001).
14. R. N. Clayton, *Annu. Rev. Earth Planet. Sci.* **21**, 115 (1993).
15. ———, L. Grossman, T. K. Mayeda, *Science* **182**, 485 (1973).
16. R. N. Clayton, N. Onuma, L. Grossman, T. K. Mayeda, *Earth Planet. Sci. Lett.* **34**, 209-224 (1977).
17. G. W. Lugmair, A. Shukolyukov, *Geochim. Cosmochim. Acta* **62**, 2863 (1998).
18. E. D. Young, R. D. Ash, P. England, D. Rumble III, *Science* **286**, 1331 (1999).
19. G. W. Wetherill, *Geochim. Cosmochim. Acta* **58**, 4513-4520 (1994).
20. W. Benz, personal communication.
21. A. N. Halliday, D. Porcelli, *Earth Planet. Sci. Lett.*, in press.
22. W. Yi *et al.*, *J. Geophys. Res.* **105**, 927 (2000).
23. R. N. Clayton, T. K. Mayeda, *Proc. Lunar Planet. Sci. Conf.* **XV**, C245 (1984).
24. J. Newton, I. A. Franchi, C. T. Pillinger, *Meteorit. Planet. Sci.* **35**, 689 (2000).

25. An early version of this manuscript benefited from reviews of R. Wieler, J. Eiler, and three anonymous reviewers. We acknowledge financial support of the Swiss National Fonds and ETH and the provision of samples by NASA.

1 June 2001; accepted 31 August 2001

Ultrathin Single-Crystalline Silver Nanowire Arrays Formed in an Ambient Solution Phase

Byung Hee Hong, Sung Chul Bae, Chi-Wan Lee, Sukmin Jeong, Kwang S. Kim*

We report the synthesis of single-crystalline silver nanowires of atomic dimensions. The ultrathin silver wires with 0.4 nanometer width grow up to micrometer-scale length inside the pores of self-assembled calix[4]hydroquinone nanotubes by electro-/photochemical redox reaction in an ambient aqueous phase. The present subnanowires are very stable under ambient air and aqueous environments, unlike previously reported metal wires of ~1 nanometer diameter, which existed only transiently in ultrahigh vacuum. The wires exist as coherently oriented three-dimensional arrays of ultrahigh density and thus could be used as model systems for investigating one-dimensional phenomena and as nanoconnectors for designing nanoelectronic devices.

Nanowires have attracted extensive interest in recent years because of their unusual quantum properties and potential use as nanoconnectors and nanoscale devices (*1*–*3*). To possess enhanced physical properties, the wires need to be of small diameter, high aspect ratio, and uniformly oriented (*2*). The stability of the nanowires is also a concern, because metal nanowires of ~1 nm diameter are reported to have existed only transiently (<10 s in ultrahigh vacuum) (*1*, *3*).

We have recently designed, synthesized, and characterized self-assembled organic nanotube arrays (Fig. 1A) formed by calix[4]hydroquinones (CHQs) (Fig. 1B) in the aqueous phase and found that they form chessboard-like arrays of rectangular pores (*4*, *5*). The macrocyclic molecule CHQ is an electrochemically active calixarene derivative with four hydroquinone (HQ) subunits

(*6*). HQs are widely used as reducing agents (*7, 8*); in particular, to reduce silver ions to form silver aggregates in acidic solution under photochemical conditions (*7*), because of the free energy gain through the reduction-oxidation process (*9*). The inner surface of the pores in the CHQ nanotubes is composed of aromatic π faces and OH groups. In the aqueous phase, partially mobile water molecules are present inside the pores because of the hydrophilic OH groups of CHQs and the water molecules bridging CHQ monomers, and thus help stabilize the silver ions in the pores. In particular, the rich π-electron density of HQ moieties in the CHQ nanotubes enables the CHQ nanotubes to capture metal ions in their pores with high affinity by cation-π interactions (*10–12*). Because the reduced neutral silver atoms do not exhibit strong interactions with the HQ moieties, they readily aggregate into nanowires (Fig. 1, C and D), as the size of the pores closely matches the primitive cell structure of

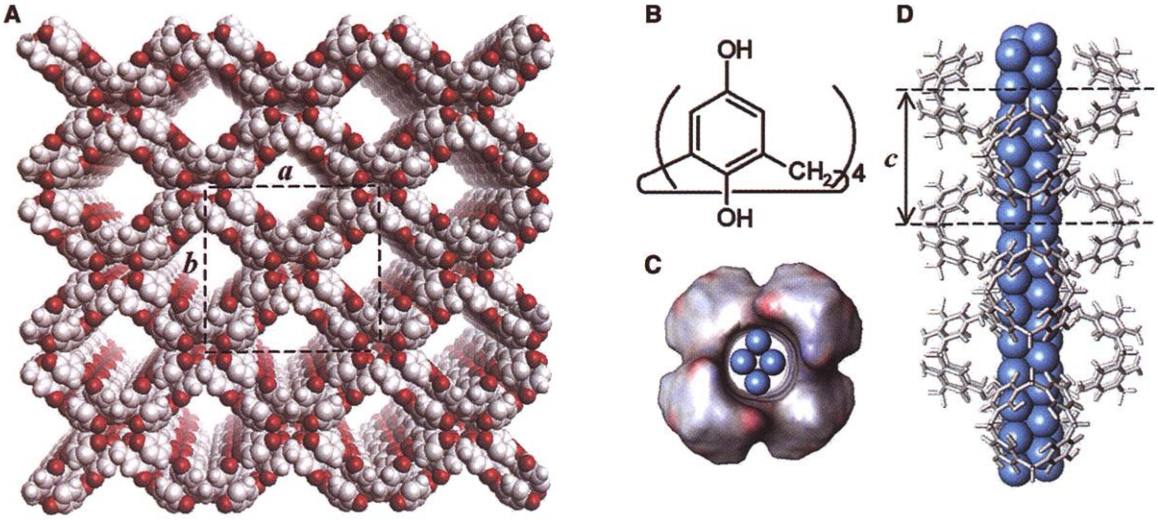

Fig. 1. Organic nanotube templates and a silver nanowire inside the nanotube. (**A**) A schematic view of CHQ nanotube arrays based on the x-ray analysis (*4*) of the crystal (orthorhombic, space group Cmmm with lattice constants: $a = 2.50$ nm, $b = 2.33$ nm, $c = 1.16$ nm and $\alpha = \beta = \gamma = 90°$) reveals that the pores of 0.6 × 0.6 nm2 (with van der Waals volume excluded) are separated by 1.7 nm from the neighboring ones. Water molecules are not shown for clarity. O atoms are shown in red. (**B**) CHQ monomer. (**C** and **D**) Top and side views, respectively, of a silver nanowire inside a CHQ nanotubetemplate. The solvent-accessible surface model in (C) and the stick model in (D) show schematic views of the CHQ nanotubes. The red color of the surface represents the negative electrostatic potential on oxygen atoms. The space-filled models (blue) represent the silver nanowires.

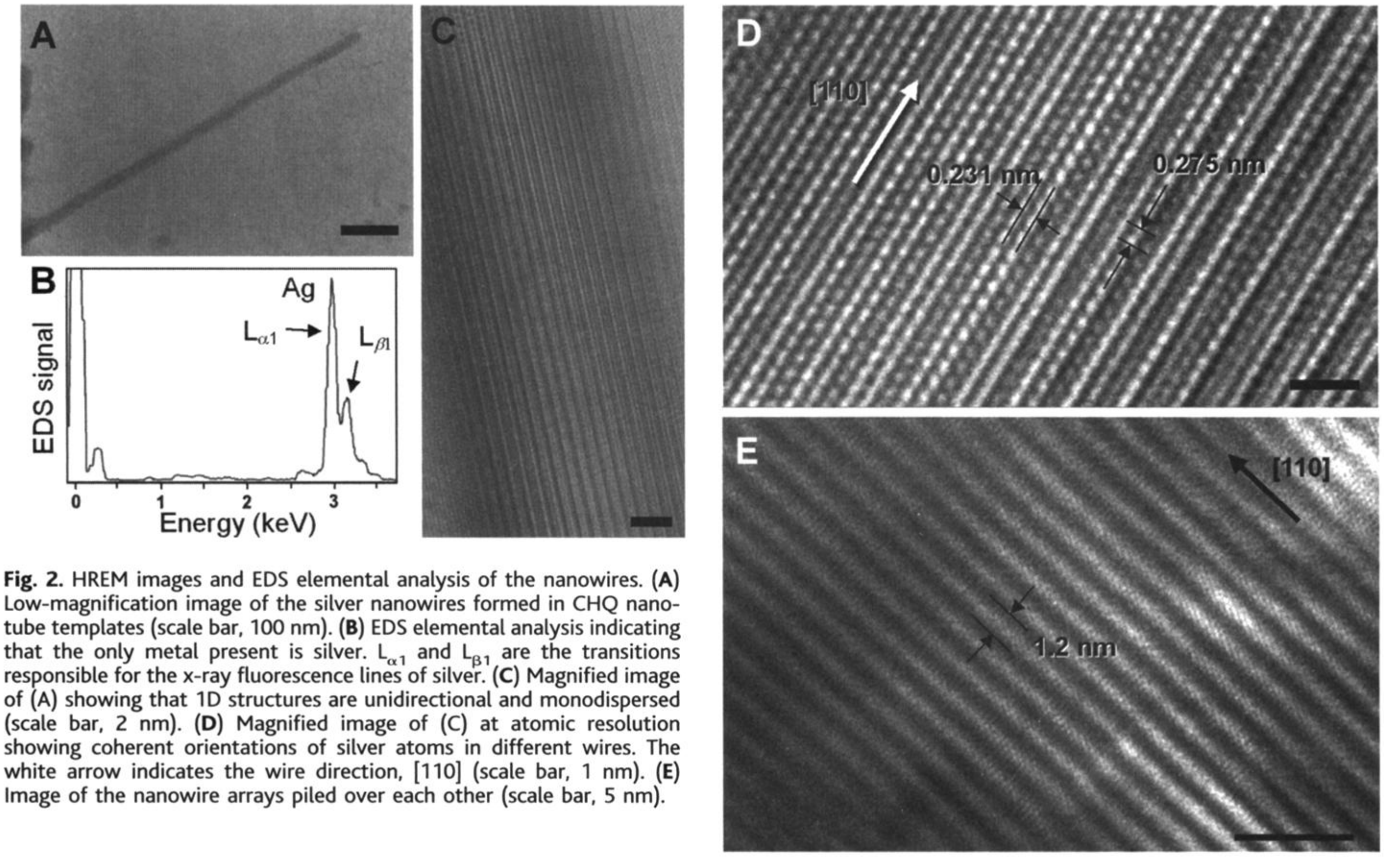

Fig. 2. HREM images and EDS elemental analysis of the nanowires. (**A**) Low-magnification image of the silver nanowires formed in CHQ nanotube templates (scale bar, 100 nm). (**B**) EDS elemental analysis indicating that the only metal present is silver. $L_{\alpha 1}$ and $L_{\beta 1}$ are the transitions responsible for the x-ray fluorescence lines of silver. (**C**) Magnified image of (A) showing that 1D structures are unidirectional and monodispersed (scale bar, 2 nm). (**D**) Magnified image of (C) at atomic resolution showing coherent orientations of silver atoms in different wires. The white arrow indicates the wire direction, [110] (scale bar, 1 nm). (**E**) Image of the nanowire arrays piled over each other (scale bar, 5 nm).

National Creative Research Initiative Center for Superfunctional Materials, Department of Chemistry, Division of Molecular and Life Sciences, Pohang University of Science and Technology, Hyojadong, Namgu, Pohang 790-784, Korea.

*To whom correspondence should be addressed. E-mail: kim@postech.ac.kr

the face-centered cubic (fcc) lattice of the bulk silver.

To prepare the nanowires, the CHQ nanotube powder was soaked in a 1 M $AgNO_3$ aqueous solution for a few minutes, followed by ultraviolet irradiation for 30 s to accelerate the redox process. The resulting product was filtered and rinsed with distilled water. All the processes were carried out in the solution phase at standard temperature and pressure, whereas most of the previous methods involved extreme conditions such as high temperature (*13*), high pressure (*2*), or high vacuum (*3*).

High-resolution electron microscope (HREM) images (*14*) and energy-dispersive x-ray spectroscopy (EDS) analysis of the silver nanowires in the CHQ nanotube bundles, together with the x-ray structure of the CHQ nanotube crystal, reveal that single-crystalline and monodispersed silver nanowires 0.4 nm in width are formed inside the pores of the CHQ nanotube arrays (Figs. 2 and 3). The EDS analysis shows that the nanowires are composed only of silver atoms (Fig. 2B). Because the organic elements of the CHQ nanotubes do not exhibit characteristic patterns in HREM imaging at 200 keV, the visible patterns (Fig. 2, C through E) emerge solely from the silver atoms. Figure 2C shows that the one-dimensional (1D) arrays are unidirectional and monodispersed. The uniformity of the HREM image of the nanowires was found up to a length of ~750 nm, indicating the well-ordered 1D structure (*15*). The spots and lines in the HREM image (Fig. 2D) represent the positions of the silver atoms or lattice. The atomic spacing along the wire axis ([110] direction) is 0.275 nm (Fig. 2D), which is 5% shorter than the corresponding value of the fcc bulk along the [110] direction (0.289 nm). From the HREM image of the nanowire arrays piled over each other, the periodicity of 1.7 nm from axis to axis of neighboring wires is observed, as in Fig. 2E, where the distance between adjacent black stripes (1.2 nm) corresponds to the projected view of the pore-to-pore distance of CHQ nanotube arrays on the (*110*) plane in terms of the nanowire array reference basis ($1.7\ \mathrm{nm}/\sqrt{2} = 1.2\ \mathrm{nm}$) (*16*). This indicates the well-ordered 3D arrays of ultrahigh density. Two different types of indexing are used: the silver fcc lattice (shown in roman text) and the nanowire array reference basis (shown in italic text) (Fig. 3, A through C) (*17*).

The electron diffraction (ED) patterns of the HREM images, together with the image simulation, show that the silver nanowires are uniformly aligned within the pores of the CHQ nanotube bundles (Fig. 3, D through I). The analysis of the nanowire arrays along the [*212*] direction (Fig. 3, D through F) confirms the existence of single-crystalline silver nanowires. Although the 1D structures within carbon nanotubes have been characterized as either individual wires or as polydispersed and twisted bundles (*18–20*), the present silver nanowires samples are observed as coherently oriented arrays that show wire-wire periodicity as well as atomic periodicity. In Fig. 3D, the distance from the origin to the lattice point $3\ \bar{4}\ \bar{1}$ is 3.64 nm^{-1}, corresponding to the reciprocal of the distance between two neighboring silver atoms, whereas the distance from the origin to the nearest lattice point $\bar{1}$ 20 is 1.32 nm^{-1}, corresponding to the reciprocal of the distance between two neighboring wires (0.76 nm) in Fig. 3E (*21*). Therefore, the figure exhibits a unique 3D wire-array ED pattern, showing lines of spots in the direction perpendicular to the wire axis (Fig. 3D). This pattern is somewhat similar to the case of MoS_2 nanotube arrays (*22*). We have also observed other ED pattern images that demonstrate the existence of 3D wire arrays [see the supplementary material (*23*)]. The single-crystalline pattern of deformed hexagonal symmetry also matches the calculated pattern with the zone axis [*453*], with an error of only 2% (Fig. 3, G through I). The low-index orientation of the nanowire arrays exhibits pseudo bulk-like patterns (Fig. 3, G and H), which cannot be observed from any possible orientations of the bulk (fcc) silver crystal (*21*). Figure 3G, obtained from a small section of the clear 1D wire arrays shown at low magnification in Fig. 3J, indicates that the deformed hexagonal pattern originates from the array architectures. In addi-

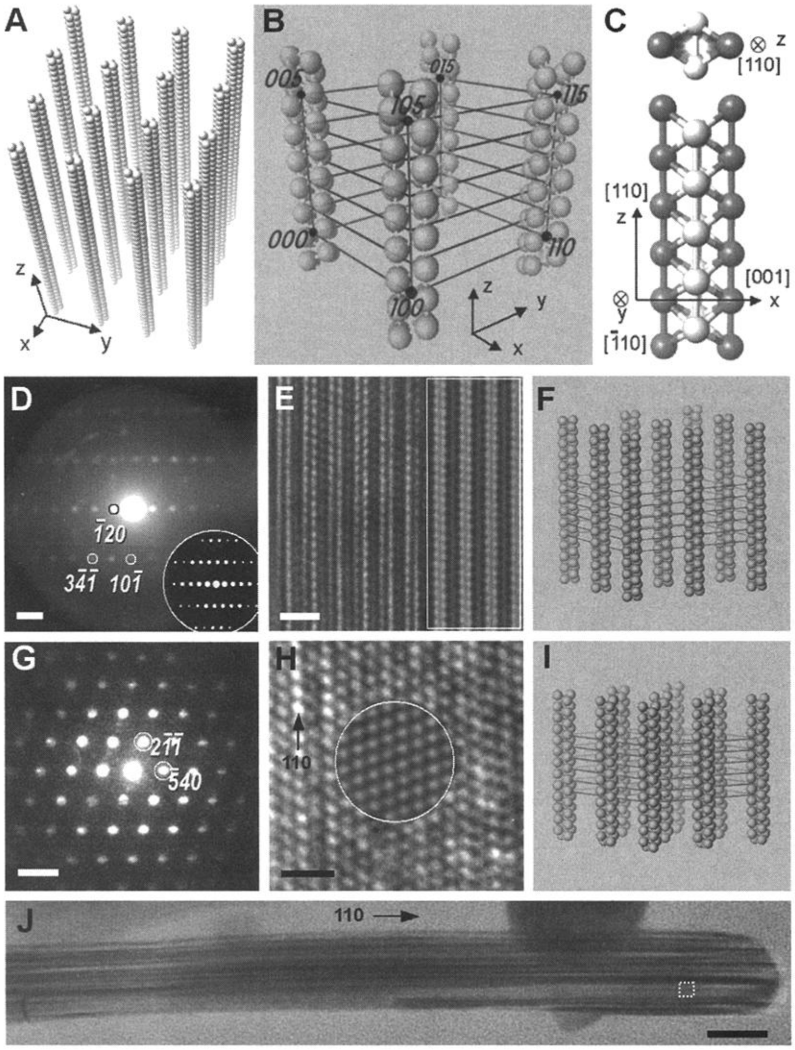

Fig. 3. Structural analysis of the single-crystalline primitive silver nanowire arrays. **(A)** 3D model of the 4 × 4 silver nanowire arrays. The *z* axis corresponds to the [110] direction of the fcc lattice. **(B)** Zone axis notations (in italics) in terms of the nanowire array reference basis. The [*100*], [*010*], and [*001*] directions in this wire array reference basis correspond to [001], [$\bar{1}$10], and [110] of the fcc lattice, respectively. **(C)** Top and side views of a primitive silver nanowire model. **(D)** Selected area diffraction pattern for zone [*212*] (scale bar, 2 nm^{-1}) and simulated pattern (inset). **(E)** HREM image (scale bar, 1 nm) and simulated image (inset; sample thickness = 17 nm, defocus = 70 nm) corresponding to (D). **(F)** Nanowire array orientation corresponding to (E). **(G)** Nano–beam diffraction pattern for zone [*453*] (scale bar, 5 nm^{-1}). **(H)** HREM image (scale bar, 1 nm) and simulated image (inset; sample thickness = 17 nm, defocus = 80 nm) corresponding to (G). **(I)** Nanowire array orientation corresponding to (H). **(J)** HREM image of a nanotube bundle with nanowires inside the pores (scale bar, 10 nm). Image (H) is the highly magnified HREM image of the dotted square shown in (J).

tion, the HREM images do not show the surface reconstruction observed in gold nanobridges (*24*) and nanorods (*25*). Thus, all HREM images provide affirmative evidence that the silver structures exist as nanowires but not as bulk or electroplated surfaces. In particular, Figs. 2D, 3E, and 3H demonstrate the uniformly oriented 3D arrays with coherent orientations of silver atoms in neighboring wires (*26*).

The geometrical structures of the nanowires available from HREM images are compared with theoretical results, which we also used to investigate the electronic structure. We have carried out density-functional electronic structure calculations (*27*), using the ultrasoft pseudopotential plane wave method (*28*). A supercell was used, so that the neighboring nanowires were sufficiently separated. The calculated atomic layer spacing along the [110] wire axis (0.278 nm) was 4% smaller than the corresponding calculated bulk value (0.289 nm), which is in good agreement with the HREM result (0.275 nm). The interatomic spacing along the [001] direction was determined to be 0.395 nm, which is 3% smaller than the corresponding bulk value (0.409 nm). A slightly more substantial compression of the interatomic distances is observed across the cross section rather than along the wire axis. This is due to increased interactions between the inner and surface atoms caused by the high electron density near the surfaces in the case of metals, which has also been observed in silver nanoclusters (*29*). The calculated electronic structure shown in Fig. 4 suggests that the silver nanowire is metallic (*30*). The *s* bands cross the Fermi level at three points, suggesting the existence of three conducting channels for electronic transport as a quantum wire. On the other hand, the calculation predicts that the CHQ nanotube is an insulator (with a ~3 eV band gap), which shields the conduction between nanowires.

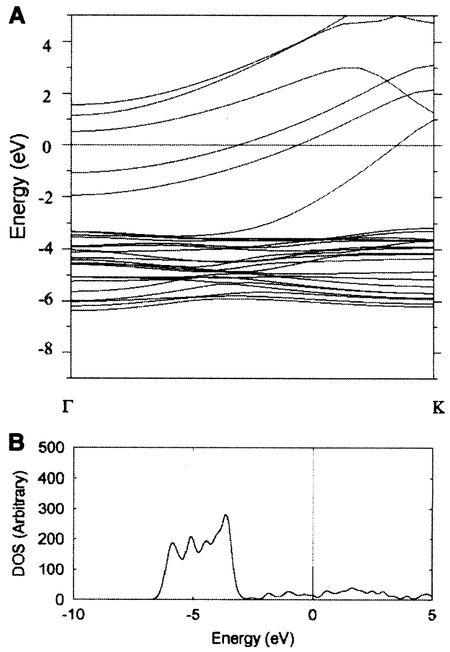

Fig. 4. Electronic band structure (**A**) and density of states (DOS) (**B**) of the single-crystalline primitive silver nanowire along the [110] direction.

Because the silver nanowires are confined and protected by the organic supporter, the shielding effect prevents them from oxidizing. In addition, the organic supporter provides long-term stability for the ultrathin linear nanowires, which would otherwise show only transient stability. In the samples stored under ambient air or aqueous environments for more than a month, no notable changes have been observed in the analysis of FTIR spectra and HREM images. Finally, considering the oxidation potential of the HQ moieties in the CHQ and the reduction potentials of metal ions, it should be possible to prepare nanowires in a similar way with other metallic elements, such as gold, palladium, platinum, and mercury.

References and Notes

1. A. I. Yanson, G. R. Bollinger, H. E. van der Brom, N. Agraït, J. M. van Ruitenbeek, *Nature* **395**, 783 (1998).
2. J. D. Holmes, K. P. Johnston, R. C. Doty, B. A. Korgel, *Science* **287**, 1471 (2000).
3. Y. Kondo, K. Takayanagi, *Science* **289**, 606 (2000).
4. B. H. Hong *et al.*, *J. Am. Chem. Soc.*, in press.
5. Under ambient conditions, 0.1 g of CHQ monomer dissolved in 50 ml of 1:1 water:acetone solution, which led to the formation of nanotube bundles as the acetone dried up. In the presence of cesium sulfate, the bundles grew into needlelike dark brown crystals. The x-ray structure of the crystal has been deposited in the Cambridge Crystallographic Data Centre as supplementary publication no. CCDC-161593. The inner surface of the CHQ nanotube is composed of hydroquinone (HQ) moieties framed by four 1D H-bond arrays formed with OH groups of quinones and water molecules. The nanotube bundles are formed by π-π stacking interactions between HQ moieties of nanotubes. The simple view of the inner surface can be seen in Fig. 1D and the supplementary material (*23*), and the more detailed views of the molecular structure around the pores, as well as the details of x-ray and infrared characterization of the CHQ nanotubes, are available in (*4*).
6. M. Gómez-Kaifer, P. A. Reddy, C. D. Gutsche, L. Echegoyen, *J. Am. Chem. Soc.* **116**, 3580 (1994).
7. E. Braun, Y. Eichen, U. Sivan, G. Ben-Yoseph, *Nature* **391**, 775 (1998).
8. T. A. Taton, C. A. Mirkin, R. L. Letsinger, *Science* **289**, 1757 (2000).
9. Once the silver cations are captured inside the pores, the redox process between Ag^+ and CHQ takes place spontaneously because the reduction potential (E°) is positive (0.1 V): $Ag^+ + e^- \rightarrow Ag$ ($E^\circ = 0.8$ V) and $Q + 2H^+ + 2e^- \rightarrow HQ$ ($E^\circ = 0.7$ V), where Q is the quinone moiety. The number of Ag atoms is half of the maximum reduction sites of the CHQ nanotubes.
10. D. A. Dougherty, *Science* **271**, 163 (1996).
11. H. S. Choi, S. B. Suh, S. J. Cho, K. S. Kim, *Proc. Natl. Acad. Sci. U.S.A.* **95**, 12094 (1998).
12. K. S. Kim, P. Tarakeshwar, J. Y. Lee, *Chem. Rev.* **100**, 4145 (2000).
13. M. P. Zach, K. H. Ng, R. M. Penner, *Science* **290**, 2120 (2000).
14. The HREM images were obtained with a 200-keV JEOL JEM-2010F microscope.
15. More extensive versions of the electron microscope images are available in the supplementary material (*23*).
16. We have also observed the HREM images of the stripe-to-stripe distance of ~0.7 nm, corresponding to the projected wire-wire distance on the (*210*) plane [see supplementary material (*23*)].
17. In the nanowire array reference basis, it should be noted that the distance from the origin to the [*001*] direction (0.275 nm) is much shorter than that from the origin to the [*100*] and [*010*] directions (1.7 nm).
18. R. M. Meyer *et al.*, *Science* **289**, 1325 (2000).
19. D. Ugarte, A. Chatelain, W. A. de Heer, *Science* **274**, 1897 (1996).
20. L. Henrard, A. Loiseau, C. Journet, P. Bernier, *Eur. Phys. J.* **13**, 661 (2000).
21. In Fig. 3E, the projected distance between two neighboring wires on the (*212*) plane is 0.76 nm [$= 1.7\ \mathrm{nm}/(2^2 + 1^2)^{1/2}$]. In Fig. 3H, that on the (*453*) plane is 0.265 nm [$= 1.7\ \mathrm{nm}/(4^2 + 5^2)^{1/2}$]. The distance from the origin to the lattice point $\bar{5}40$ is 3.77 nm^{-1}, corresponding to the reciprocal distance between two neighboring wires [$(0.265\ \mathrm{nm})^{-1}$]. This is contrasted to the reciprocal distance [$(0.236\ \mathrm{nm})^{-1} = 4.24\ \mathrm{nm}^{-1}$] observed in the bulk silver along the [110] direction.
22. M. Remskar *et al.*, *Science* **292**, 479 (2001).
23. Supplementary Web material is available on Science Online at www.sciencemag.org/cgi/content/full/1062126/DC1.
24. Y. Kondo, K. Takayanagi, *Phys. Rev. Lett.* **79**, 3455 (1997).
25. Z. L. Wang, R. P. Gao, B. Nikoobakht, M. A. El-Sayed, *J. Phys. Chem. B* **104**, 5417 (2000).
26. The silver nanowires, which have the fcc primitive cell structure, are aligned with uniform orientations (Fig. 3B). In the case of CHQ nanotubes, the O atoms of water molecules bridging neighboring CHQs are nearest to the pore axis (~0.28 nm), whereas atoms of CHQs are somewhat far from the pore axis (~0.4 nm). Once inside the pores and reduced, the silver atoms interact with the nonmobile bridging water molecules, leading to the coherent orientation of silver atoms in neighboring nanowires. Although some of the H-bonding structure in the pore is changed by the formation of the silver wire, the overall skeletal structure of the nanotube arrays is determined by the π-π stacking. Thus, the overall structure of the CHQ tube arrays with silver nanowires is not substantially different from that of the pure CHQ nanotube arrays. This is evidenced from experiments showing that the pore-to-pore distance in the x-ray structure of the nanotube arrays and the wire-to-wire distance in the HREM structure of the nanowire arrays inside the nanotube bundles are practically the same. We have also seen many other HREM patterns that show that well-oriented nanowires form in the pores of the CHQ nanotube arrays [a few of them are in the supplementary material (*23*)].
27. D. M. Ceperley, B. J. Alder, *Phys. Rev. Lett.* **45**, 566 (1980).
28. D. Vanderbilt, *Phys. Rev. B* **41**, 7892 (1990).
29. J. Yoon, K. S. Kim, K. K. Baeck, *J. Chem. Phys.* **112**, 9335 (2000).
30. We have investigated the electron energy-loss spectroscopy (EELS) in HREM for both the bulk and nanowires [see supplementary material (*23*)]. In the nanowires, the volume plasmon peak at 7.4 eV corresponding to the bulk almost disappears, but a weak peak at ~6 eV seems to appear, although it is not clearly resolved because of the strong zero-loss peak. Furthermore, when the samples are exposed to the electron beam of HREM, we find that the silver wires in the supports are stable. This is possibly due to high conductivity, because less conductive palladium wires (which have a higher boiling point) tend to evaporate because of local heating. This supports the idea that the silver wires are conductive. The contact problem needs to be solved for the direct measurement of the conductivity.
31. Supported by Korea Institute of Science and Technology Evaluation and Planning (Creative Research Initiative) and partly by Brain Korea 21. We thank C. G. Park, S. G. Hong, K. W. Cho, B. I. Kang, B. W. Seo, Pohang University of Science and Technology (POSTECH), G. S. Park, M. Kim (SAIT), and J. C. Park (Hynix Co.) for HREM, FE-SEM, and EELS analyses; S. J. Youn for calculations; and S. Granick, J.-M. Zuo (Univ. of Illinois), H. J. Lee, S. Lee, and J. Chung (POSTECH) for discussion.

1 May 2001; accepted 27 August 2001
Published online 6 September 2001;
10.1126/science.1062126
Include this information when citing this paper.